Journal of Applied Fluid Mechanics , Vol. 9, No. 1, pp. 487-499, 2016.
Available online at www.jafmonline.net, ISSN 1735-3572, EISSN 1735-3645.
DOI: 10.18869/acadpub.jafm.68.224.23934

CFD Simulations of Pressure Drop and Velocity Field in a Cyclone Separator with Central Vortex Stabilization Rod

J.J.H. Houben[1†], Ch. Weiss[2], E. Brunnmair[3] and S. Pirker[1]

[1] *Johannes Kepler University Linz, Altenbergerstrasse 69, 4040 Linz, Austria*
[2] *Montanuniversitaet Leoben, Franz-Josef-Strasse 18, 8700 Leoben, Austria*
[3] *Bublon GmbH, Grazer Straße 19-25, 8200 Gleisdorf, Austria*

† *Corresponding Author Email*: *j.j.h.houben@gmail.com*

(Received July 8, 2014; accepted December 3, 2014)

ABSTRACT

A problem of cyclone separators is the low grade efficiency of small particles. Therefore, a high efficiency cyclone separator has been developed and successfully tested in former work. In this cyclone separator, a vortex stabilizer is used to suppress the vortex core precession. In this article, the pressure and flow field in this cyclone separator are calculated by means of computational fluid dynamics using the commercial software Ansys Fluent 13. The position of the vortex core is tracked in these simulations by searching the position of minimal dynamic pressure and the centre of moment of the horizontal velocity components as function of the axial coordinate. The results are compared with experimental data. It is demonstrated that when using a stabilizer, the vortex is kept in position. Furthermore the maximum of the tangential velocity is found to be larger, which is known to have a positive effect on the separation of small particles in the inner solid body rotation vortex.

Keywords: Computational Fluid Dynamics; preceeding vortex core; cyclone separator; pressure drop.

NOMENCLATURE

$\bar{p}$	time averaged pressure	cb	cyclone body
p'	time fluctuating pressure	i	counter
$C_{1\varepsilon}$; $C_{2\varepsilon}$; C_μ	numerical constants	in	inlet
C_1; C_2; C_1'; C_2'	numerical constants	o	outlet
C_{ij}	convection term	P	near wall point
D	diameter	r	rod
D_H	hydraulic diameter	rad	radial
$D_{T,ij}$	turbulent diffusion	rel	relative
$D_{L,ij}$	molecular diffusion	tan	tangential
E	empirical constant	tot	total
F_{ij}	production term	vf	vortex finder
f	frequency	vfi	vortex finder inner
G_k	generation of turbulence	I_{turb}	turbulent intensity
G_{ij}	buoyancy	St	Strouhal number
k	turbulent kinetic energy	ε	turbulent dissipation rate
L_c	natural vortex length	κ	von Kármán constant
M	velocity moment	μ	dynamic viscosity
P_{ij}	stress production	μ_t	turbulent viscosity
t	time	ν	kinematic viscosity
ax	axial	ϕ_{ij}, $\phi_{ij,1}$, $\phi_{ij,2}$, $\phi_{ij,w}$	pressure strain terms
c	cone, centre	ρ	density
h	horizontal	τ_w	wall shear stress

1. INTRODUCTION

Although their introduction is more than a century ago, cyclone separators are still widely used in industry. This because of their robustness, low production and running costs and high temperature and pressure resistance. The design should allow a maximal separation efficiency combined with a minimal pressure drop. Also a high selectivity between the over- and underflow is desired. However, particles smaller than roughly 1 μm in diameter are still hard to separate with a standard cyclone and other complementary technologies are needed, such as electrostatic precipitators, bag and fiber filters, venturi scrubbers or rotating particle separators (Brouwers (2002)). These technologies are however more expensive in both investment and operation costs.

From the middle of the last century, many research has been performed on (semi)empirical models to predict the velocity distribution, the pressure drop and the separation efficiency in cyclone separators. Pioneering work in this field was performed Shephered and Lapple (1939). In the fifties Barth (1956) developed the cut size theory, which predicts the particle diameter that is separated with a probability of 50%. Barth's theory was further improved for higher solid loadings by Muschelknautz (1970) and Trefz and Muschelknautz (1993) and is nowadays one of the most widely used analytical models (Muschelknautz et al. (1997)). For a recent and complete overview of existing models the reader is referred to e.g. Cortés and Gil (2007), which also provides an overall picture of computational fluid dynamics (CFD) used for cyclone separators, starting from Boysan et al. (1982). From a comparison to laser doppler measurements, it is known that only the Reynolds Averaged Navier-Stokes Reynolds Stress Model or (lattice Boltzmann) Large Eddy Simulation give reasonable numerical results (e.g. Gronald and Derksen (2011)). Since the latter method has high computational costs, the newest developments go into direction of hybrid models that are able to resolve critical regions finer (e.g. Pirker et al. (2013)).

One of the problems in cyclone separator design is that, in contradiction to most mathematical models, longer cyclones do not automatically have a better separation efficiency (Hoffmann and Stein (2007)). In these cases the vortex core does not reach the bottom of the cyclone but will bend before to the wall. This phenomenon is known as the end of the vortex (EOV), where the distance between the entrance of the vortex finder and the height where the vortex touches the wall is defined as the natural vortex length.

Three models from literature to estimate this natural vortex length are listed in Tab. 2 and are compared with the distance available in the test cyclone, i.e. between the entrance of the vortex finder and the disc near the dust outlet (see Fig. 1(a)). All three models predict a longer natural vortex length than the distance available in the geometry and therefore no EOV may be expected.

Another character of many cyclone designs is that the movement of the vortex' centre is not stationary in the cyclone's axis, which is called the precessing vortex core (PVC) by Derksen and Van den Akker (2000). This non-stationary behaviour influences the cyclone's pressure drop and separation efficiency in a negative way. The frequency, f, of the vortex core may be defined by a dimensionless Strouhal number, St, as function of the body diameter D_c and the inlet velocity v_{in} according to Eq. (1) (Peng et al. (2005)):

$$\mathrm{St} = \frac{f D_c}{v_{in}}. \tag{1}$$

The St number is known to be more or less independent of the volume flow rate and can be stated to be a function of the geometry only. In literature values between 0.4 and 0.6 are mentioned (Hoekstra et al. (1999), Peng et al. (2005)), which would give a PVC-frequency of 8 and 60 Hz for volume flow rate of 200 and 1500 m^3/h respectively for the cyclone geometry in this study.

Brunnmair et al. (2009) developed a new type of cyclone with a higher separation efficiency for small particles, which was successfully tested in experiments. Features of this cyclone are the high and small logarithmic inlet and the central rod (described for the first time by Staudinger et al. (1992)), which stabilises the inner vortex and prevents it from precessing. Due to the last, the separation zone is divided into one for large particles, located at the outer wall, and a second one in the cyclone's centre around the rod separating smaller particles. The tangential velocity component of the vortices in these two regions is described with Eq. (2)

$$v_{tan} \cdot r^n = \mathrm{const}, \tag{2}$$

where n takes the value -1 to describe the solid inner vortex and ca. 0.7-0.8 for the outer free Rankine vortex (Meißner and Löffler (1978), Hoffmann et al. (2001)). Brunnmair et al. (2009) found the maximal tangential velocity to be higher with the use of a rod. This higher tangential velocity would

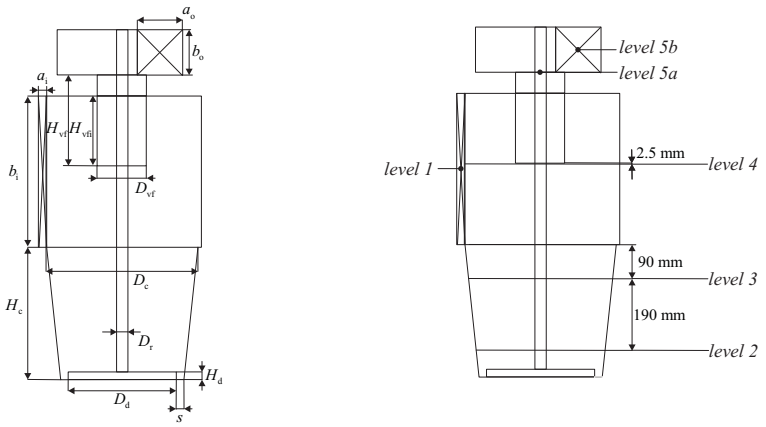

(a) Cyclone dimensions as listed in table 1. (b) Definition of measurement levels.

Fig. 1. Cyclone dimensions and measurement levels.

Table 1. Cyclone dimensions as sketched in Fig. 1(a).

quantity	symbol	value	unit
inlet width	a_{in}	0.022	m
inlet height	b_{in}	0.400	m
outlet width	a_o	0.120	m
outlet height	b_o	0.120	m
cone top diameter	D_c	0.400	m
vortex finder diamter	D_{vf}	0.130	m
rod diamter	D_r	0.030	m
disc diamter	D_d	0.286	m
cone heigth	H_c	0.350	m
vortex finder total length	H_{vf}	0.222	m
vortex finder inner length	H_{vfi}	0.185	m
disc height	H_d	0.002	m
dust outlet gap	s	0.020	m

Table 2. Models to calculate the natural vortex length, L_c, and its values for the test cyclone's geometry with: D_{vf}, the vortex finder diameter, D_{cb}, the diameter of the cyclone body (without spiral inlet) and a_{in} and b_{in}, the width and height of the inlet respectively. The vertical distance between the bottom of the vortex finder and the disc near the dust outlet equals 0.563 m (further cyclone dimensions are defined in Fig. 1(a)).

Author	Equation	L_c [m]
Alexander 1949 (Hoffmann et al. (1995))	$\frac{L_c}{D_{cb}} = 2.3\frac{D_{vf}}{D_{cb}}\left(\frac{D_{cb}^2}{a_{in}b_{in}}\right)^{1/3}$	0.786
Bryant et al. 1983 (Qian and Zhang (2005))	$\frac{L_c}{D_{cb}} = 2.26\left(\frac{D_{vf}}{D_{cb}}\right)^{-1}\left(\frac{D_{cb}^2}{a_{in}b_{in}}\right)^{-0.5}$	0.652
Zhongli et al. 1991 (Hoffmann et al. (1995))	$\frac{L_c}{D_{cb}} = 2.4\left(\frac{D_{vf}}{D_{cb}}\right)^{-2.25}\left(\frac{D_{cb}^2}{a_{in}b_{in}}\right)^{-0.361}$	4.225

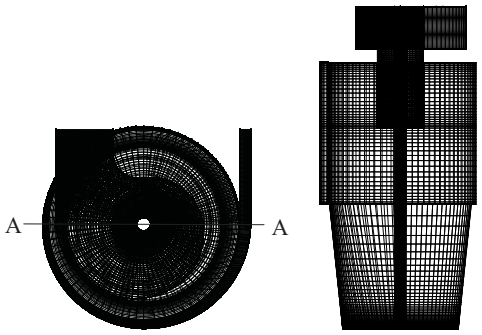

Fig. 2. The cyclones computational grid top view (left) and front view (right).

cause higher centrifugal forces on smaller particles and therefore a higher total separation efficiency.

In this article the effect of the use of such a stabilisation rod is demonstrated by comparing the results of CFD-simulations with pitot tube and manometer measurements of Brunnmair (2010). Furthermore results of the simulations provide a closer look to the vortex precession which gives insights that have not been noticed during the experiments.

2. NUMERICAL INVESTIGATIONS

Simulations were performed with the commercial software package Ansys Fluent 13 (Fluent (2005)) on a desktop with Intel® Core™ i5-2450M CPU with 2.50 GHz and 4.00 RAM.

2.1 Computational mesh

The mesh shown in Fig. 2, was created in Gambit and consists of hexahedral and polyhedral cells. The 235 640 polyhedral cells were converted from a paved mesh. They are only present in the second half of the outlet spiral, located downstream, because of the geometry of this outlet spiral. The mesh of the lower part of the cyclone is structured. For the mesh of the geometry without rod, the cells in the centre axis form a cuboid, which prevents highly skewed cells. The total number of cells is 759 470 for the geometry *with* and 852 910 without rod.

2.2 Conservative laws

The considered fluid velocities in the experiments of Brunnmair et al. (2009) are much smaller (maximal $< 100\,\mathrm{m\,s^{-1}}$) than the speed of sound of this fluid under the same conditions ($\approx 340\,\mathrm{m\,s^{-1}}$), i.e. pressure and temperature. Therefore the Mach-number is much smaller than unity (Ma ≈ 0.3, and the flow can be treated as incompressible (Nieuwstadt (1998)). The equations for continuity then becomes:

$$\frac{\partial \bar{u_\mathrm{i}}}{\partial x_\mathrm{i}} = 0. \tag{3}$$

Since the medium considered to be incompressible and is known to be a Newtonian fluid, for momentum the Navier-Stokes equations have been taken as basis:

$$\rho \frac{\partial u_\mathrm{i}}{\partial t} + \rho u_\mathrm{j} \frac{\partial u_\mathrm{i}}{\partial x_\mathrm{j}} = \rho g_\mathrm{i} - \frac{\partial p}{\partial x_\mathrm{i}} + \mu \frac{\partial^2 u_\mathrm{i}}{\partial x_\mathrm{j}^2}. \tag{4}$$

The fluid velocity components u_i and u_j are known to be turbulent and fluctuating in time for the flow in cyclone separators (Gronald and Derksen (2011)) and Eq. (4) is therefore solved using Reynolds Averaged Navier Stokes (RANS) modelling described in the sections below.

Energy conservation laws are further not taken into account since the experiments of Brunnmair (2010) were carried at ambient conditions, without any heat fluxes due to temperature gradients.

2.3 Turbulence modelling

Since the flow in a cyclone is strongly swirled, the Reynolds stress model (RSM) is used to account for anisotropic turbulence. The RSM model is known to give reasonable results for industrial applications (Gronald and Derksen (2011), Talbi et al. (2011)). However, in order to get stable final RSM-simulation results the standard $k-\varepsilon$ model was used for the first iteration steps.

2.31 Standard $k-\varepsilon$ model

In the standard $k-\varepsilon$ model, two differential equations for the turbulent kinetic energy k and the turbulent dissipation rate ε are considered, having the following general form (Fluent (2005)):

$$\frac{\partial}{\partial t}(\rho k) + \frac{\partial}{\partial x_\mathrm{i}}(\rho k u_\mathrm{i}) = \tag{5a}$$
$$\frac{\partial}{\partial x_\mathrm{j}}\left[\left(\mu + \frac{\mu_\mathrm{t}}{\sigma_\mathrm{k}}\right)\frac{\partial k}{\partial x_\mathrm{j}}\right] + G_\mathrm{k} + G_\mathrm{b} - \rho\varepsilon - Y_\mathrm{M} + S_\mathrm{k},$$

$$\frac{\partial}{\partial t}(\rho \varepsilon) + \frac{\partial}{\partial x_\mathrm{i}}(\rho \varepsilon u_\mathrm{i}) = \tag{5b}$$
$$\frac{\partial}{\partial x_\mathrm{j}}\left[\left(\mu + \frac{\mu_\mathrm{t}}{\sigma_\varepsilon}\right)\frac{\partial \varepsilon}{\partial x_\mathrm{j}}\right] + C_{1\varepsilon}\frac{\varepsilon}{k}(G_\mathrm{k} + C_{3\varepsilon}G_\mathrm{b}) - C_{2\rho}\frac{\varepsilon^2}{k}S_\varepsilon,$$

where

$$\mu_\mathrm{t} = \rho C_\mu \frac{k^2}{\varepsilon} \tag{6}$$

is the turbulent viscosity. The generation of turbulence is calculated as follows:

$$G_{\mathrm{k}} = -\rho\overline{u_{\mathrm{i}}' u'}\mathrm{j}\frac{\partial u_{\mathrm{j}}}{\partial x_{\mathrm{i}}}. \tag{7}$$

The generation of turbulent energy due to buoyancy G_{b} is not taken into account for isothermal flows such as the dilatation dissipation Y_{M}, which is only important for flows with higher Ma-numbers, and any user-defined source terms S_{k} and S_{ε} for the turbulent kinetic energy and dissipation rate respectively. The constants in Eq. (5) have the following numerical values in this study: $C_{1\varepsilon} = 1.44$, $C_{2\varepsilon} = 1.92$, $C_{\mu} = 0.09$, $\sigma_{\mathrm{k}} = 1.0$, $\sigma_{\varepsilon} = 1.3$, the latter two being the turbulent Prandtl number for k and ε respectively.

2.32 Reynolds stress model RSM

The transport equations of the Reynolds stresses $\rho\overline{u_{\mathrm{i}}' u_{\mathrm{j}}'}$ are written in the following general form:

$$\frac{\partial}{\partial t}\left(\rho\overline{u_{\mathrm{i}}' u_{\mathrm{j}}'}\right) + C_{\mathrm{ij}} = D_{\mathrm{T,ij}} + D_{\mathrm{L,ij}} + P_{\mathrm{ij}} + G_{\mathrm{ij}} + \phi_{\mathrm{ij}} - \varepsilon_{\mathrm{ij}} + F_{\mathrm{ij}}, \tag{8}$$

representing the following terms from left to right: local time derivative; C_{ij}: convection; $D_{\mathrm{T,ij}}$: turbulent diffusion; $D_{\mathrm{L,ij}}$: molecular diffusion; P_{ij} stress production: G_{ij} buoyancy; ϕ_{ij}: pressure strain; $\varepsilon_{\mathrm{ij}}$: dissipation; F_{ij}: production by system rotation. No modeling is needed for the convection, the molecular diffusion, the stress production and the production by system rotation, whereas the buoyancy production equals zero for isothermal flow. The remaining terms are closed by the following equations (Fluent (2005)):

$$D_{\mathrm{T,ij}} = \frac{\partial}{\partial x_{\mathrm{k}}}\left(\frac{\mu_{\mathrm{t}}}{\sigma_{\mathrm{k}}}\frac{\partial \overline{u_{\mathrm{i}}' u_{\mathrm{j}}'}}{\partial x_{\mathrm{k}}},\right) \tag{9}$$

where $\sigma_{\mathrm{k}} = 0,82$ (Lien and Leschziner (1994)). The pressure strain is modelled linear using the following decomposition:

$$\phi_{\mathrm{ij}} = \phi_{\mathrm{ij},1} + \phi_{\mathrm{ij},2} + \phi_{\mathrm{ij,w}} \tag{10}$$

with, when ignoring system rotation and buoyancy:

$$\phi_{\mathrm{ij},1} = -C_1\rho\frac{\varepsilon}{k}\left[\overline{u_{\mathrm{i}}' u_{\mathrm{j}}'} - \frac{2}{3}\delta_{\mathrm{ij}}k\right], \tag{11a}$$

$$\phi_{\mathrm{ij},2} = -C_2\left[\left(P_{\mathrm{ij}} + -C_{\mathrm{ij}}\right) - \frac{2}{3}\delta_{\mathrm{ij}}\left(P - C\right)\right], \tag{11b}$$

$$\begin{aligned}\phi_{\mathrm{ij,w}} = {} & C'_1\frac{\varepsilon}{k}\left(\overline{u_{\mathrm{k}}' u_{\mathrm{m}}'}n_{\mathrm{k}}n_{\mathrm{m}}\delta_{\mathrm{ij}} - \frac{3}{2}\overline{u_{\mathrm{i}}' u_{\mathrm{k}}'}n_{\mathrm{j}}n_{\mathrm{k}}\right. \\ & \left. - \frac{3}{2}\overline{u_{\mathrm{j}}' u_{\mathrm{k}}'}n_{\mathrm{i}}n_{\mathrm{k}}\right)\frac{C_{\mathrm{l}}k^{3/2}}{\varepsilon d} \\ & + C'_2\left(\phi_{\mathrm{km},2}n_{\mathrm{k}}n_{\mathrm{m}}\delta_{\mathrm{ij}} - \frac{3}{2}\phi_{\mathrm{ik},2}n_{\mathrm{j}}n_{\mathrm{k}}\right. \\ & \left. - \frac{3}{2}\phi_{\mathrm{jk},2}n_{\mathrm{i}}n_{\mathrm{k}}\right)\frac{C_{\mathrm{l}}k^{3/2}}{\varepsilon d}\end{aligned} \tag{11c}$$

The constants in Eq. (11) have the following numerical values: $C_1 = 1.8$; $C_2 = 0.6$; $C'_1 = 0.5$; $C'_2 = 0.3$ and $\kappa = 0.4187$ the von Kármán constant. n_{k} is the x_{k} component of the unit normal to the wall, d is the normal distance to the wall. Furthermore $P = \frac{1}{2}P_{\mathrm{kk}}$, $C = \frac{1}{2}C_{\mathrm{kk}}$ and $C_{\mathrm{l}} = C_{\mu}^{3/4}/\kappa$.

2.4 Boundary conditions

In the CFD simulations the following boundary conditions were set in Fluent Ansys (Fluent (2005)):

- inlet: velocity inlet
- outlet: pressure outlet
- wall: standard wall function

The details of these boundary conditions are discussed in the sections below.

2.41 Inlet

The velocity of the fluid is assumed to have a block profile with a magnitude of the ratio of the volume flow rate and the area of the inlet. Turbulence is calculated by the hydraulic diameter D_{H} and the turbulent intensity, which is calculated with (Houben (2011)):

$$I_{\mathrm{turb}} = 0.16\mathrm{Re}_{\mathrm{H}}^{-1/8} \tag{12}$$

with the Reynolds number based on the hydraulic diameter

$$\mathrm{Re}_{\mathrm{H}} = \frac{v_{\mathrm{in}}D_{\mathrm{H}}}{\nu}. \tag{13}$$

For the Reynolds stress specification method k or the turbulent intensity are used.

2.42 Outlet

Since the outlet in the experiments of Brunnmair (2010) is of the spiral type, no problems with back flow into the domain were expected, which was confirmed during simulations. Therefore, no geometry adaption was made, e.g. of the type of the disc (e.g Derksen (2003)). Back flow turbulent intensity was put on zero to avoid turbulence to flow back into the domain.

2.43 Wall

Standard wall functions were applied where the mean velocity is calculated with:

$$U^* = \frac{1}{\kappa}\ln(Ey^*) \qquad \text{for } y^* > 11.225 \qquad (14a)$$

$$U^* = y^* \qquad \text{for } y^* < 11.225 \qquad (14b)$$

in which the dimensionless velocity U^* and the dimensionless wall distance y^* are defined as:

$$U^* = \frac{U_P C_\mu^{1/4} k_P^{1/4}}{\tau_w/\rho} \qquad (15a)$$

$$y^* = \frac{\rho C_\mu^{1/4} k_P^{1/2} y_P}{\mu}, \qquad (15b)$$

where U_P, k_P and y_P are the mean fluid velocity, turbulent kinetic energy at the near wall point P and the distance from this near wall point to the wall respectively. Furthermore, E is an empirical constant with the value of 9.793.

The wall boundary condition from the k-equation applied meaning that

$$\frac{\partial k}{\partial n} = 0. \qquad (16)$$

For the production of k and the turbulent dissipation rate the following equations are used:

$$G_k = \frac{\tau_w^2}{\kappa\rho C_\mu^{1/4} k_P^{1/2} y_P} \qquad (17a)$$

$$\varepsilon = \frac{C_\mu^{3/4} k_P^{3/2}}{\kappa y_P}. \qquad (17b)$$

2.5 Discretization schemes

The velocity-pressure coupling was performed with the SIMPLE algorithm with the PRESTO! pressure discretization scheme, whereas the discretization of momentum, turbulent kinetic energy, dissipation rate and Reynolds stresses were achieved with the QUICK scheme.

2.6 Vortex core tracking

During the same time the centre of the vortex is determined by dividing the cylindrical and conical part into 11 levels of axial coordinate. For saving computational effort and for achieving a high resolution, the velocities were only tracked on circles with diameters twice as large as that of the vortex finder. The resolution of the x and y-velocity sampling data was 5.2 mm in both x and y directions. The moment of inertia by these two velocity components around the cyclone's vertical axis is computed with:

$$M_u = \sum_{i=1}^{N} u_i \cdot y_i \qquad (18a)$$

$$M_v = \sum_{i=1}^{N} v_i \cdot x_i, \qquad (18b)$$

where u_i and v_i are the velocity components in x and y direction respectively and x_i and y_i the coordinates for each local grid point, with index i. The centre of the vortex is then determined to the point (x_c, y_c) where the cumulative sum the moment of inertia of both velocity components is half of the total moment of inertia of these velocities:

$$\sum_{i=1}^{x=x_c} v_i \cdot x_i = M_{v,c} = \frac{M_v}{2}, \qquad (19a)$$

$$\sum_{i=1}^{y=y_c} u_i \cdot y_i = M_{u,c} = \frac{M_u}{2}. \qquad (19b)$$

Also the position of the vortex core was calculated, where the absolute value of the horizontal velocities has a minimum value:

$$v_h = \sqrt{v_x^2 + v_y^2}. \qquad (20)$$

Under the assumption that the z-velocity remains constant in the observed area, this point corresponds with the point of minimal dynamic pressure,

$$p_{dyn} = \frac{1}{2}\rho\left(u^2 + v^2 + w^2\right) \qquad (21)$$

and therefore with the vortex core.

2.7 Computational time and convergence

Calculations were started with the smallest volume flow rate of 200 m^3/h and $k-\varepsilon$ as turbulence model using 3 of 4 available CPU's. For checking convergence, the statical pressures on the in- and outlet of the cyclone separator as well on the lower and

upper cross sectional area of the vortex finder were monitored. After 1 000 iteration steps and approximately 1 hour real time, monitored pressures became stable and the turbulence model was changed to RSM, for which another 9 000 iteration steps were performed taking approx. 15 hours real time. Then the solver mode was changed from steady to unsteady using a time step of 0.01 s and maximal 50 iterations per time step. After 100 time steps, taking circa 8 hours, pressure monitors results were written during another 100 time steps. During another 100 equal time steps, the velocity components and pressure monitors were averaged during 1 s flow time.

The vortex core tracking was achieved using one single CPU and using 11 user defined functions, i.e. one for each horizontal cross sectional area. Time for achieving 0.01 s real time and writing out the data for after 50 iterations was 10 and 5 minutes respectively. I.e. collecting data for 1 s real time took 25 h in total.

Quasi steady state solutions for larger volume flow rates were reached in the same starting from the steady state RSM-solution of the next smaller volume flow rate, leaving all other further steps unchanged.

3. RESULTS & DISCUSSION

The pressure drop and flow velocities are compared to experimental data of Brunnmair (2010). The existence of the precessing vortex core is demonstrated with the help of the methods as described in Sec. 2.

3.1 Pressure (drop)

The total pressure, i.e. the sum of static and dynamic pressure, with and without rod are shown in Fig. 3 and are compared with experimental data. The individual pressure levels have been monitored at the inlet, the entrance and exit of the vortex finder and the exit of the spiral outlet (see Fig. 1).

The pressure drop between the inlet and the entrance of the vortex finder is slightly underpredicted in the simulations (Fig. 3(a)). Furthermore, the numerical results do not show the reduction of the pressure drop by the rod, which has been noticed during the experiments.

In the vortex finder itself, the pressure drop further increases by the high swirl in the flow (3(b)). However the increase in pressure drop is seen to be much higher during the experiments than in the simulations. The value with and without stabilisation rod do not differ very much, although also here a little tendency for a higher pressure drop when using the rod is visible in the numerical results.

After the spiral outlet the biggest difference between experimental and numerical results are noticed (Fig. 3(c)). Whereas the experimental results show a decrease in pressure drop, in the simulations the total pressure drop raises. The stabilisation rod has a comparable effect on the mean pressure drop as for the case without a spiral outlet. An explanation for the large differences between the simulations and the experimental results is the difficulty to measure a time averaged pressure due to the high turbulence induced by the trailing edge of the vortex finder and the change in flow direction.

The relative pressure drop fluctuation, defined as

$$p'_{\mathrm{rel}} = \frac{\int_{t=0}^{t_{\mathrm{end}}} \sqrt{(p-\bar{p})^2}\,\mathrm{d}t}{\int_{t=0}^{t_{\mathrm{end}}} \bar{p}\,\mathrm{d}t} \tag{22}$$

$$\bar{p} = \frac{\int_{t=0}^{t_{\mathrm{end}}} p\,\mathrm{d}t}{t_{\mathrm{end}}} \tag{23}$$

is shown in Fig 3(d) for a volume flow rate of 500 m^3/h. It is clearly noticed that the pressure fluctuates much less when a rod is used: whereas the relative fluctuating pressure without a rod is in the range of 5-8%, this value decreases to only 0-3% which indicated the vortex stabilising effect of the rod.

3.2 Flow field

The three velocity components are shown in Fig. 4 as function of the radial coordinate from the cyclones centre to the opposite of the inlet. The radial and tangential velocities are made dimensionless with the mean inlet velocity and the axial velocity with the mean axial velocity through the vortex finder. Because of the vortex core precession (Derksen and Van den Akker (2000)) the velocity components strongly fluctuate in time. This movement is due to the unsteady character of the flow, not due to turbulence. Therefore, the shown profiles are mean values for a simulation time of one second, which corresponds to approximately 20 cycles of fluctuating pressure drop for the simulated volume flow rate of 500 m^3/h acc. to Eq. (1).

For the tangential velocity a clear difference between the inner and outer zone is visible. The inner vortex is represented by a solid body rotation whereas the outer region represents a potential vortex. The maximal tangential velocity is found at a radial coordinate slightly smaller than the vortex finder diameter as observed in experiments by Brunnmair et al. (2009). As in the experiments a larger maximum for the tangential velocity is noticed in case a rod is used, which is assumed to have

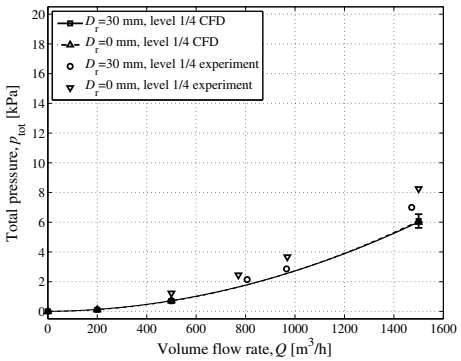

(a) Pressure drop between level 1 and 4.

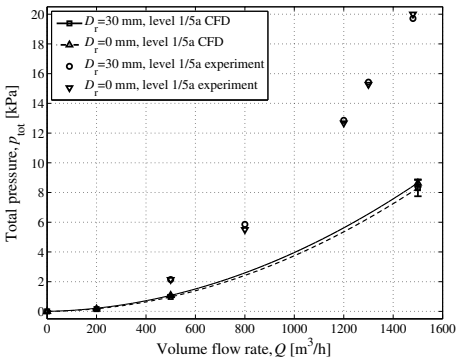

(b) Pressure drop between level 1 and 5a.

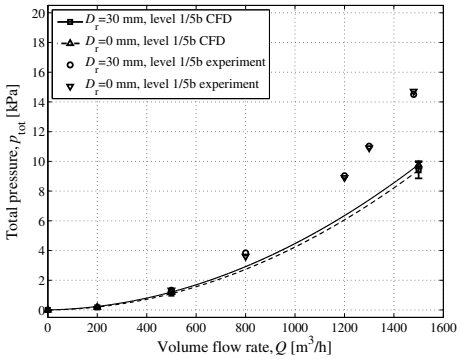

(c) Pressure drop between level 1 and 5b.

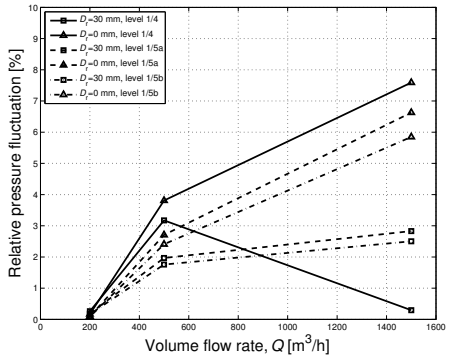

(d) Relative fluctuating pressure.

Fig. 3. Comparison of experimental and computational results of total pressure drops for the cyclone separator with and without stabilisation rod. The levels are according to Fig. 1(b).

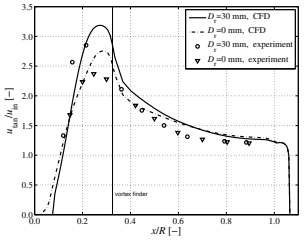

(a) Dimensionless tangential velocity at $z = 0.19$ m.

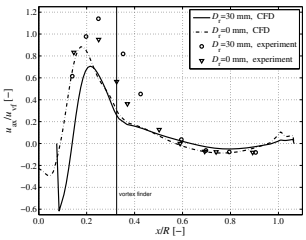

(b) Dimensionless axial velocity at $z = 0.19$ m.

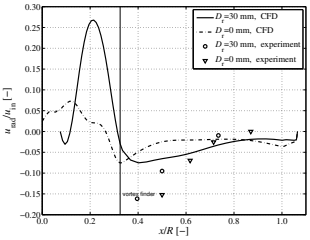

(c) Dimensionless radial velocity at $z = 0.19$ m.

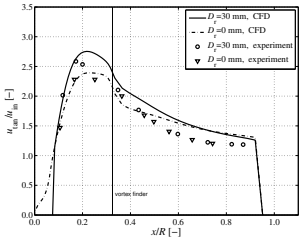

(d) Dimensionless tangential velocity at $z = -0.09$ m.

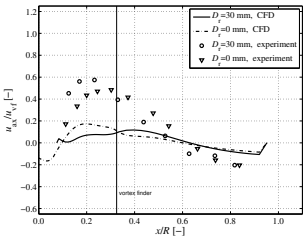

(e) Dimensionless axial velocity at $z = -0.09$ m.

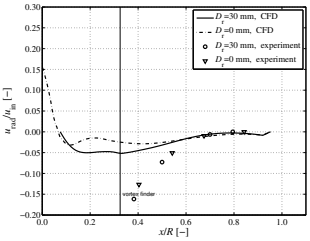

(f) Dimensionless radial velocity at $z = -0.09$ m.

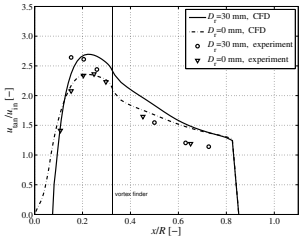

(g) Dimensionless tangential velocity at $z = -0.28$ m.

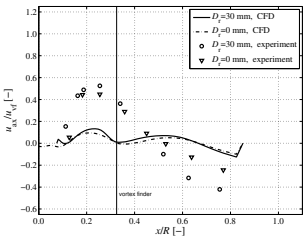

(h) Dimensionless axial velocity at $z = -0.28$ m.

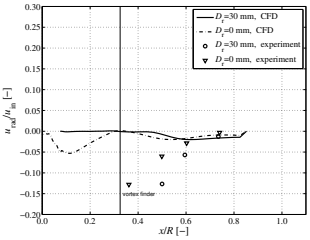

(i) Dimensionless radial velocity at $z = -0.28$ m.

Fig. 4. Comparison of CFD simulation with experimental data of Brunnmair et al. for a volume flow rate of 500 m^3/h**.**

a positive effect on the separation of fine particles in the inner vortex.

Also the axial velocity has a maximum between the stabilisation rod and the vortex finder. In the outer region the velocity in general points downwards although close the vortex finder it may also point upwards. The drop in the axial velocity below the vortex finder is also noticed in the simulations of Derksen et al. (2006). The agreement between experiments and simulations would be better in case mass loading effects are considered in stead of using one-way coupling. At the two lower levels in the cyclone, the correspondence of the experimental to the numerical values becomes less.

Close to the stabilisation rod the radial velocity points towards the centre. It becomes smaller and even negative with a minimum at the same radius of the vortex finder. This phenomena is known as lip leakage (Hoffmann and Stein (2007)) and vanishes further downwards in the cyclone. Curious is the peak of the radial velocity at the level just beneath the vortex finder, which is pointed outwards. The peak is about 4 times larger when a rod is used and could force particles outward again after they have become entrained in the secondary flow.

3.3 Precessing vortex core

In Fig. 5 the results of calculated position of the vortex core as function of the dimensionless vertical coordinate $\bar{z} = \frac{z+H_c+H_d}{H_c+b_i}$ are shown. The radial position of the vortex core r is made dimensionless by the diameter of the rod $D_r = 30$ mm. It is calculated by solving Eq. (18) and Eq. (19) for Fig. 5(a), 5(c) and 5(e) and by searching the point, where the velocity in the horizontal plane has an absolute minimum according to Eq. (20) for Fig. 5(b), 5(d) and 5(f). For obtaining the data, the velocities on 11 planes were tracked during 100 time steps of 0.01 s and 50 iterations per time step. As post processing from the simulation the mean velocity components at the radial position and their standard deviation were calculated for an averaging time interval of one second.

The use of a stabilisation rod does not seem to have much influence on the centre of moment for volume flow rates of 200 and 1500 m^3/h: the curves in both Fig. 5(a) and 5(e) intersect more than once. However, at a volume flow rate of 500 m^3/h this does not occur and the use of the rod has a positive effect on the symmetry of the vortex (Fig. 5(c)).

Fig. 5(b), 5(d) and 5(f) show that the centre of minimal pressure of the vortex does not drift away from the radius of the stabilisation rod, although it may rotate around it. The smaller deviations at the volume flow rates of 500 and 1500 m^3/h are due to numerical errors of the finite grid size. Without the rod the vortex is observed to precess. However, this precession is within a fluid volume smaller than that of the rod and from this point of view the rod's diameter seems to be over-dimensioned.

4. CONCLUSIONS AND RECOMMENDATIONS

A new type of cyclone separator has been successfully simulated by means of computational fluid dynamics and the results of this study have been compared with data from former experiments. The new type uses a central rod, which stabilises the vortex and prevents it from precessing around the cyclone's axis and from prematurely ending at the wall. Effects of the rod are:

- A more constant pressure drop, which is noticed from the numerical results. An absolute reduction in pressure drop as seen during experiments is not confirmed by the simulations. One possible reason for this could be the larger frictional area of a cyclone separator with a rod and the difficulty of experimentally measuring a time mean pressure drop in turbulent flow.
- A higher maximum of the tangential velocity profile, both noticed in experiments and simulations. The location of this maximum is at a radius a little smaller than half the vortex finder's diameter. This higher tangential velocity is assumed to have a positive effect on the separation of smaller particles in the secondary flow beneath the vortex finder.
- A decrease of the vortex core precessing. When using a stabilisation rod, the vortex core, i.e. the place of minimal dynamic pressure, is not seen to precess. However, without a rod this precession is in an area smaller than the rod's cross sectional area. This means that the diameter of the rod most probably has been oversized and a smaller rod could have the same positive effect on the PVC without the negative results on the pressure drop.

Recommendations on future work are:

- A more sophisticated turbulence model could describe the velocity profiles more realistically. This turbulence model could be used as a hybrid model where the better model is only used locally where a (much) higher resolution is desired.

Recommendations for improving the cyclone design are:

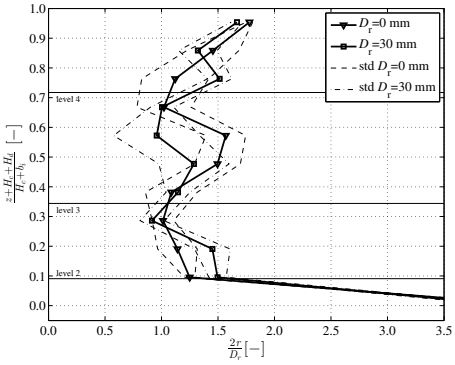

(a) $\sqrt{x_c^2+y_c^2}$ for 200 m^3/h.

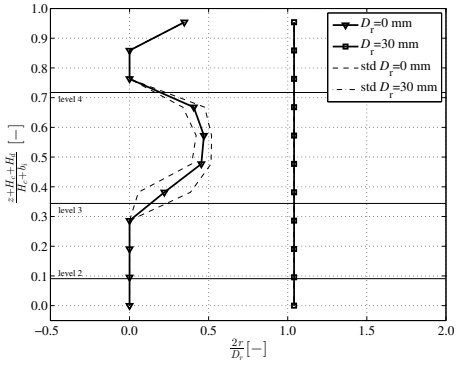

(b) $r(\min({v_x}^2+{v_y}^2),z)$ for 200 m^3/h.

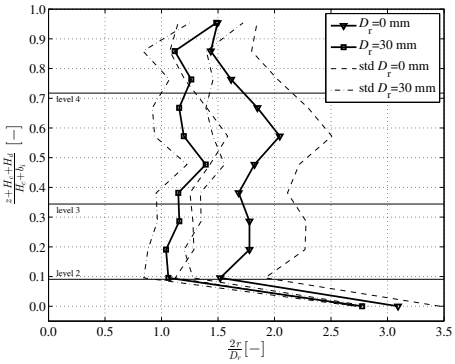

(c) $\sqrt{x_c^2+y_c^2}$ for 500 m^3/h.

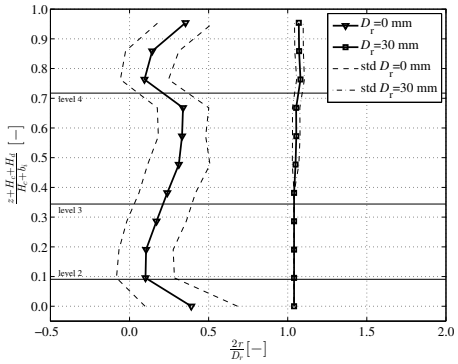

(d) $r(\min({v_x}^2+{v_y}^2),z)$ for 500 m^3/h.

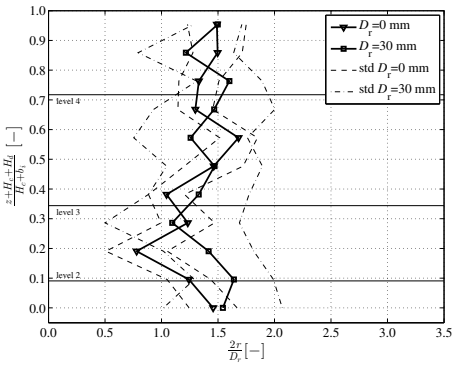

(e) $\sqrt{x_c^2+y_c^2}$ for 1500 m^3/h.

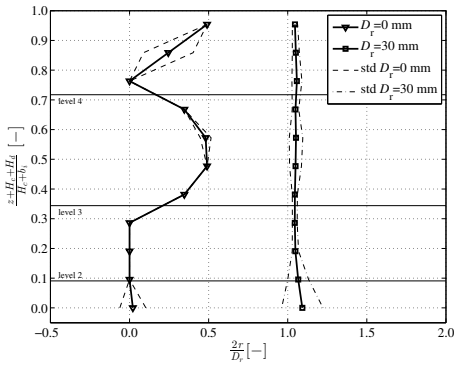

(f) $r(\min({v_x}^2+{v_y}^2),z)$ for 1500 m^3/h.

Fig. 5. Comparison of the vortex core equated from the moment of inertia (left) and minimum of dynamic pressure in the horizontal plane (right) for volume flow rates of 200, 500 and 1500 m^3/h**. The radial position of the vortex core** r **is made dimensionless by half the diameter of the rod (**$D_r = 30$mm**).**

- The use of a thinner rod, which lowers the pressure drop due to wall friction without losing the effect of stabilising the vortex.
- For a longer cyclone design the rod could even have a more positive effect since it would not only stabilise the PVC but could also elongate the natural vortex length.
- A rotating rod would raise the maximum of the tangential velocity and therefore improve the separation efficiency. Such a rotating rod could be combined with a rotating particle separator mounted on it.

REFERENCES

Barth, W. (1956). Berechnung und Auslegung von Zyklonabscheidern auf Grund neuerer Untersuchungen. *Brennstoff Wärme Kraft, 8 (1)*, 1–9.

Boysan, F., W. Ayers, and J. Swithenbank (1982). A fundamental mathematical modelling approach to cyclone design. *Transactions of the Institution of Chemical Engineers 60*(4), 222–230.

Brouwers, J. (2002). Phase separation in centrifugal fields with emphasis on the rotational particle separator. *Experimental thermal and fluid science 26*(2), 325–334.

Brunnmair, E. (2010). *Hochleistungszyklone zur Trennung von Feststoff-Gas-Gemischen*. Ph. D. thesis, Montanuniversitaet Leoben.

Brunnmair, E., F. Dunst, and H. Flachberger (2009). Neuartiger Gaszyklon mit differenzierter Grob-und Feinabtrennzone. *BHM Berg- und Hüttenmnnische Monatshefte 154*(12), 610–613.

Cortés, C. and A. Gil (2007). Modeling the gas and particle flow inside cyclone separators. *Progress in energy and combustion Science 33*(5), 409–452.

Derksen, J. (2003). Separation performance predictions of a stairmand high-efficiency cyclone. *AIChE Journal 49*(6), 1359–1371.

Derksen, J., S. Sundaresan, and H. van den Akker (2006). Simulation of mass-loading effects in gas–solid cyclone separators. *Powder technology 163*(1), 59–68.

Derksen, J. and H. Van den Akker (2000). Simulation of vortex core precession in a reverse-flow cyclone. *AIChE Journal 46*(7), 1317–1331.

Fluent (2005). *Manual Version 6.2. 16, 2005, Fluent*.

Gronald, G. and J. Derksen (2011). Simulating turbulent swirling flow in a gas cyclone: A comparison of various modeling approaches. *Powder Technology 205*(1), 160–171.

Hoekstra, A., J. Derksen, and H. Van Den Akker (1999). An experimental and numerical study of turbulent swirling flow in gas cyclones. *Chemical Engineering Science 54*(2055), 2065.

Hoffmann, A., M. De Groot, W. Peng, H. Dries, and J. Kater (2001). Advantages and risks in increasing cyclone separator length. *AIChE journal 47*(11), 2452–2460.

Hoffmann, A., R. de Jonge, H. Arends, and C. Hanrats (1995). Evidence of the 'natural vortex length' and its effects on the separation efficiency of gas cyclones. *Filtration & Separation 32*(8), 799–804.

Hoffmann, A. and L. Stein (2007). *Gas Cyclones and Swirl Tubes: Principles, Design, and Operation*. Springer Verlag.

Houben, J. J. H. (2011). *Experimental investigations and CFD simulations on particle depositions in gas cyclone separators*. Ph. D. thesis, Montanuniversitaet Leoben.

Lien, F.-S. and M. Leschziner (1994). Assessment of turbulence-transport models including non-linear RNG eddy-viscosity formulation and second-moment closure for flow over a backward-facing step. *Computers & Fluids 23*(8), 983–1004.

Meißner, P. and F. Löffler (1978). Zur Berechnung des Strömungsfeldes im Zyklonabscheider. *Chemie Ingenieur Technik 50*(6), 471.

Muschelknautz, E. (1970). Auslegung von Zyklonabscheidern in der technischen Praxis. *Staub und Reinhaltung der Luft 30*(5), 187–195.

Muschelknautz, E., V. Greif, and M. Trefz (1997). *VDI-Wärmeatlas*, Chapter Zyklone zur Abscheidung von Feststoffen aus Gasen, pp. Lja 1–11. VDI-Wärmeatlas Düsseldorf.

Nieuwstadt, F. (1998). Turbulentie. *Theorie en toepassingen van turbulente stromingen. Epsilon Uitgaven*.

Peng, W., A. Hoffmann, H. Dries, M. Regelink, and L. Stein (2005). Experimental study of the vortex end in centrifugal separators: The nature of the vortex end. *Chemical Engineering Science 60*(24), 6919–6928.

Pirker, S., C. Goniva, C. Kloss, S. Puttinger, J. Houben, and S. Schneiderbauer (2013). Application of a hybrid lattice boltzmann–finite volume turbulence model to cyclone

short-cut flow. *Powder Technology 235*(2), 572–580.

Qian, F. and M. Zhang (2005). Study of the natural vortex length of a cyclone with response surface methodology. *Computers and Chemical Engineering 29*(10), 2155–2162.

Shephered, C. and C. Lapple (1939). Flow pattern and pressure drop in cyclone dust collectors. *Industrial & Engineering Chemistry 31*(8), 972–984.

Staudinger, G., M. Klupak, and J. Keuschnigg (1992). Zyklone mit Zentralkörpern. *Chemie Ingenieur Technik 64*(9), 852–853.

Talbi, K., Z. Nemouchi, A. Donnot, and N. Belghar (2011). An experimental study and a numerical simulation of the turbulent flow under the vortex finder of a cyclone separator. *Journal of Applied Fluid Mechanics 4*(1).

Trefz, M. and E. Muschelknautz (1993). Extended cyclone theory for gas flows with high solids concentrations. *Chemical Engineering & Technology 16*(3), 153–160.